

Turning Night into Day: The Creation and Validation of Synthetic Nighttime Visible Imagery Using the Visible Infrared Imaging Radiometer Suite (VIIRS) Day–Night Band (DNB) and Machine Learning

CHANDRA M. PASILLAS^{a,b}, CHRISTIAN KUMMEROW,^a MICHAEL BELL,^a AND STEVEN D. MILLER^{c,a}

^a Department of Atmospheric Science, Colorado State University, Fort Collins, Colorado

^b Air Force Institute of Technology, Wright Patterson Air Force Base, Wright-Patterson, Ohio

^c Cooperative Institute for Research in the Atmosphere, Fort Collins, Colorado

(Manuscript received 16 January 2023, in final form 29 April 2024, accepted 8 May 2024)

ABSTRACT: Meteorological satellite imagery is a critical asset for observing and forecasting weather phenomena. The Joint Polar Satellite System (JPSS) Visible Infrared Imaging Radiometer Suite (VIIRS) Day–Night Band (DNB) sensor collects measurements from moonlight, airglow, and artificial lights. DNB radiances are then manipulated and scaled with a focus on digital display. DNB imagery performance is tied to the lunar cycle, with the best performance during the full moon and the worst with the new moon. We propose using feed-forward neural network models to transform brightness temperatures and wavelength differences in the infrared spectrum to a pseudo-lunar reflectance value based on lunar reflectance values derived from observed DNB radiances. JPSS NOAA-20 and *Suomi National Polar-Orbiting Partnership* (*SNPP*) satellite data over the North Pacific Ocean at night for full moon periods from December 2018 to November 2020 were used to design the models. The pseudo-lunar reflectance values are quantitatively compared to DNB lunar reflectance, providing the first-ever lunar reflectance baseline metrics. The resulting imagery product, Machine Learning Nighttime Visible Imagery (ML-NVI), is qualitatively compared to DNB lunar reflectance and infrared imagery across the lunar cycle. The imagery goal is not only to improve upon the consistent performance of DNB imagery products across the lunar cycle, but ultimately to lay the foundation for transitioning the algorithm to geostationary sensors, making global continuous nighttime imagery possible. ML-NVI demonstrates its ability to provide DNB-derived imagery with consistent contrast and representation of clouds across the full lunar cycle for nighttime cloud detection.

SIGNIFICANCE STATEMENT: This study explores the creation and evaluation of a feed-forward neural network to generate synthetic lunar reflectance values and imagery from VIIRS infrared channels. The model creates lunar reflectance values typical of full moon scenes, enabling quantifiable comparisons for nighttime imagery evaluations. Additionally, it creates imagery that highlights low clouds better than its infrared counterparts. Results indicate the ability to create visually consistent nighttime visible imagery across the full lunar cycle for the improved nighttime detection of low clouds. Wavelengths chosen are available on both polar and geostationary satellite sensors to support the utilization of the algorithm on multiple sensor platforms for improved temporal resolution and greater simultaneous geographic coverage over polar orbiters alone.

KEYWORDS: Atmosphere; Clouds; Remote sensing; Satellite observations; Machine learning

1. Introduction

Since its inception, satellite imagery has proved an invaluable resource for operational weather forecasters and atmospheric science researchers and is critical in areas with limited surface observations such as coastal regions or open oceans. Forecasters obtain timely and actionable global atmospheric data for observing and predicting hazardous weather conditions through satellite imagery. Cloud and moisture patterns of varying size and time scales are particularly beneficial for making predictions or putting model forecasts into context. Detecting clouds, especially low clouds, at night is more challenging than in the daytime due to the absence of visible imagery from solar reflectance and because of the low thermal contrast between the clouds and underlying surface in the infrared (IR) spectrum (Ellrod 1995). The Visible Infrared

Radiometer Suite (VIIRS) Day–Night Band (DNB) sensor captures radiance measurements utilizing lunar illumination and ambient light sources; however, most DNB-based imagery quality is tied to the lunar cycle. Furthermore, due to the nature of polar orbiters, on which the VIIRS DNB resides, significant lags in revisit time depending on the geographic location of the area of interest may decrease its use for some forecasting elements and time scales. More readily accessible nighttime visible imagery products that are consistent across the lunar cycle can improve forecasters' situational awareness of clouds at night, especially outside of the polar regions.

This paper proposes to use machine learning methods with IR channels and DNB lunar reflectance values to create pseudo-lunar reflectance values and associated nighttime imagery products, the Machine Learning Nighttime Visible Imagery (ML-NVI). Unlike most DNB scaling methods or previous machine learning methods for nighttime visible imagery creation, it creates a synthetic lunar reflectance value

Corresponding author: Chandra M. Pasillas, chandra.pasillas@colostate.edu, chandra.pasillas@afit.edu

that can be used for quantitative evaluation against lunar reflectance values directly calculated from sensor-measured values. The values and associated digital imagery created from ML-NVI are not an exact translation of lunar reflectance as seen in the DNB for all clouds as it also identifies thin cirrus which is not captured in traditional DNB lunar reflectance but provides a similar product that performs better than its IR counterparts. Unlike in IR where cold cirrus masks lower-level features, ML-NVI detects, but presents a transparent appearance of, some upper-level clouds that enable greater fidelity of lower-level clouds, visually accentuating low-level cloud features to the user. Created and validated using only Joint Polar Satellite System (JPSS) VIIRS channels, model input channels were selected to be transferable to channels on geostationary satellites in order to gain temporal resolution and increase simultaneous spatial coverage. The model is trained, validated, and tested using the [Miller and Turner \(2009\)](#) DNB lunar reflectance as the predictand, permitting both qualitative and quantitative nighttime assessments.

The remainder of this paper delves into the development, validation, testing, and evaluation of the ML-NVI model. [Section 2](#) provides essential background information on topics critical to understanding the problem set and development of the algorithm. [Section 3](#) highlights data selection and processing. [Section 4](#) focuses on model architecture selection and parameter tuning, resulting in a preferred model scheme. This scheme is then utilized to create three distinct models based on different latitude ranges that are then qualitatively and quantitatively compared with independent datasets for use with VIIRS in [section 5](#). [Section 5](#) also compares performance over different lunar reflectance ranges and over the full lunar cycle for the model of choice. [Section 6](#) provides case studies for fog and tropical cyclone events that occur outside of the initial training, testing, and validation regions, as well as conclusions.

2. Background

a. Infrared cloud detection at night

Visible imagery is especially helpful to forecasters as it offers the highest spatial resolution and presents clouds in a way that matches an analyst's intuition as it is similar to how clouds are observed by the human eye ([Kidder and Vonder Haar 1995](#)). Visible imagery provides contextual clues on cloud formations in the way of optical depth and texture. This makes it one of the "most easily interpreted type of satellite products ([Kidder et al. 2000](#)). Due to the lack of solar reflectance, with the exception of data from the DNB, there is no readily available nighttime visible imagery, and in its absence, forecasters must rely on IR imagery for nighttime cloud detection. Near-surface clouds have similar brightness temperatures (BTs) at IR wavelengths as Earth's surface beneath making it difficult to detect these clouds ([Ellrod 1995](#)). Physical temperature inversions make the detection of low clouds even more challenging ([Kidder and Vonder Haar 1995; Liou 2002; Chapman and Gasparovic 2022](#)). At the pixel level, multispectral techniques prove to be more useful for cloud

detection over single channels as they account for the property differences in clouds at different wavelengths ([Ellrod 1995](#)). Differences between wavelengths highlight low-level cloud features best, and cloud spectral properties can be capitalized on through the use of BT differences (BTDs) in addition to BT values when creating new cloud detection products ([Calvert and Pavoloni 2010](#)).

Many previous studies have shown the benefits of using BTDs or multispectral imagery for cloud property determination ([Prabhakara et al. 1988; Inoue 1989; Strabala et al. 1994; Ellrod 1995; Anthis and Cracknell 1999; Kidder et al. 2000; Bendix 2002; Ellrod and Gultepe 2007; Hillger 2008; Calvert and Pavoloni 2010; Lindsey et al. 2014; Kim and Hong 2019; Miller et al. 2022](#)). [Inoue \(1989\)](#) demonstrated that combining single-wavelength temperature thresholds and BTDs leads to better performance than threshold or multispectral differencing techniques alone. Later, [Strabala et al. \(1994\)](#) compared the 8–11- μm BTD and the 11–12- μm BTD and developed a tool to determine whether there was cloud present and what phase cloud it was (helping to indicate cloud height and type) based on these two values. Low cloud split window (SW) approaches typically use the 3.9- and 10.7–11.2- μm channels ([Ellrod 1995; Bendix 2002; Ellrod and Gultepe 2007; Calvert and Pavoloni 2010; Miller et al. 2022](#)). This split window technique capitalizes on the difference in spectral response functions in the IR as well as the fact that the 3.9 μm is a combination of reflected and emitted radiation. The shortwave albedo or "fog product" of the 1990s GOES satellites used the 10.7–3.9- μm BTD and revolutionized "fog and liquid water cloud detection at night" ([Kidder et al. 2000](#)). The 10.7–3.9- μm BTD remains one of the most commonly used tests for low cloud detection at night. Though these methods have greatly enhanced cloud detection at night, they do not compare to that of visible imagery, and thus, the Operational Line Scanner (OLS) and DNB were created to leverage moonlight for feature detection ([Kidder and Vonder Haar 1995; Miller et al. 2006](#)).

b. Lunar illumination

The National Aeronautics and Space Administration (NASA) has observed the spectral irradiance and radiance of the moon since 1996, and lunar radiometric models from these data are used to calibrate onboard sensors of satellites ([Kieffer and Stone 2005](#)). [Miller and Turner \(2009\)](#) published a dynamic lunar spectral irradiance dataset and model which expedited calculations of irradiance, making it possible to calculate a lunar reflectance value (between 0 and 1) for all measured DNB radiances. This enables quantitative studies of the DNB for conducting comparison calculations similar to those done with data in the visible spectrum. [Min et al. \(2017\)](#) evaluated nighttime reflectance changes from these irradiances and determined that value differences are less than 0.05% for water clouds between lunar phase angles. This demonstrated that a DNB-based nighttime cloud retrieval will have minimal impacts quantitatively due to the lunar phase, though visually it may present as vastly different. Replicating these reflectance values at full moon can provide measurements that

can be further exploited in cloud detection algorithms and imagery.

Nighttime visible imagery gained significant popularity after the development of the DNB. The DNB sensor enables radiance collection from 5 to 0.9 μm and can capture more detailed cloud features at night than longwave infrared (LWIR) (Miller et al. 2013; Min et al. 2017). The DNB sensor is currently only available on polar orbiters, thus only providing limited benefits to phenomena that evolve rapidly outside of the polar regions. It is very sensitive to low levels of light and uses a three-step gain system to detect radiances over eight orders of magnitude, utilizing lunar illumination and even air glow as its light source for nighttime imagery and full sun for daytime solar illumination (Miller et al. 2013; Liang et al. 2014; Seaman and Miller 2015; Seaman et al. 2015; Zinke 2017; Line et al. 2018). Normalizing this range for visual presentation is often challenging, and all DNB radiances must be scaled postprocessing to create imagery usable by the human eye (Zinke 2017). Further details on the DNB can be found in the Algorithm Theoretical Basis Document (ATBD) (Line et al. 2018) or the User's Guide (Seaman et al. 2015).

Three DNB scaling algorithms used to view imagery from measured DNB radiances are near-constant contrast (NCC), high and NCC (HNCC), and erf-dynamic scaling (EDS) (Liang et al. 2014; Seaman and Miller 2015; Zinke 2017). The NCC creates a pseudo-albedo (Liang et al. 2014; Seaman and Miller 2015), the HNCC creates a normalized radiance value (Zinke 2017), and the EDS creates a dynamic scaling of the radiances (Seaman and Miller 2015). These products are enhancements to make static images appear to have uniform illumination regardless of the lunar or solar influences on the viewed scene (Liang et al. 2014; Seaman and Miller 2015; Zinke 2017; Hoesel et al. 2023). In addition to differences between the products, imagery from the full moon versus a new moon for the same product will appear vastly different for similar features, leading to different interpretations of the same feature as the lunar cycle progresses (Liang et al. 2014; Seaman and Miller 2015; Zinke 2017; Hoesel et al. 2023). Furthermore, in all of these methods, users rely on postprocessed imagery, which limits them to qualitative validation with visual inspections or comparisons; depending on the specific scaling chosen by a user to highlight different features, products like the NCC can appear visually different based on the maximum and minimum values permitted by the user in the scaled image (Seaman and Miller 2015; Zinke 2017; Line et al. 2018).

c. Machine learning for nighttime visible imagery

A number of techniques have been developed in recent years to create synthetic nighttime “visible” imagery from IR channels (Chirokova et al. 2023, 2018; Kim and Hong 2019; Kim et al. 2019, 2020; Mohandoss et al. 2020; Harder et al. 2020). Many of these seek to exploit relationships seen in the IR wavelengths with daytime visible imagery (Kim and Hong 2019; Kim et al. 2019, 2020; Mohandoss et al. 2020; Harder et al. 2020). Proxy-visible imagery from the Cooperative Institute for Research of the Atmosphere (CIRA) uses scaled

VIIRS DNB radiances as truth and multiple linear regression to create its imagery. Proxy visible is used operationally by the National Hurricane Center (NHC) to aid in tropical storm tracking at night (Chirokova et al. 2023, 2018). Qualitative evaluation of these models has been predominantly in comparison with daytime visible images or nighttime IR (Kim and Hong 2019; Kim et al. 2019, 2020; Mohandoss et al. 2020; Harder et al. 2020). Quantitative metrics have been based on pattern evaluation and structural similarities versus data from observed measurements.

3. Data

a. Dataset

1) GENERAL

All satellite data used for this research included VIIRS sensor data records (SDRs) and geolocation data for bands M13–M16 and the DNB band from the JPSS NOAA-20 and *Suomi National Polar-Orbiting Partnership* (SNPP). Lin and Cao (2019) demonstrated that the relative spectral responses (RSRs) in the IR spectrum for VIIRS on these satellites are not identical, differing between 0.18 and 0.06 K. However, this minimal difference in sensor sensitivities is within documented performance limits, and thus, data from VIIRS off both systems were included when creating the training and validation datasets. Additionally, although there are both seasonal and latitudinal variations of the standard atmospheric profile causing differing RSRs in the temporal and spatial regions of study, we chose to accept these differences as within reasonable limits for data. Both of these assumptions allow us to create a model product for use in all seasons and with both satellites.

2) AREA OF INTEREST

As seen in Fig. 1, the area of interest (AOI) used for the training and validation datasets, as well as the primary testing dataset, extends from 0° to 50°N and from 180° to 127°W. This AOI was chosen to minimize complications from artificial lights and vegetation differences over land. Equivalent IR channel BTs in different geographic regions (seasons) may be tied to significantly different features: in one region (season), it may represent underlying sea surface temperatures (SSTs) and clear skies, but in another region (season), it may represent an area that is obscured by upper-level cirrus or by low-lying uniform fog. To account for various background SSTs, which range on average between 5° and 30°C in this region over the course of the year, and better capture these differences in BTs for similar features, the AOI (0°–50°N) was further divided into two subsets by latitude range (0°–30°N, 30°–50°N) seen in Fig. 1 as subregions C and B, respectively.

3) TRAINING AND VALIDATION DATASETS

The training and validation datasets were comprised of descending node VIIRS passes over the open northern Pacific Ocean from December 2018 to November 2019 that corresponded to an equatorial pass of 0130 LST on the night of the full moon \pm 1 night.

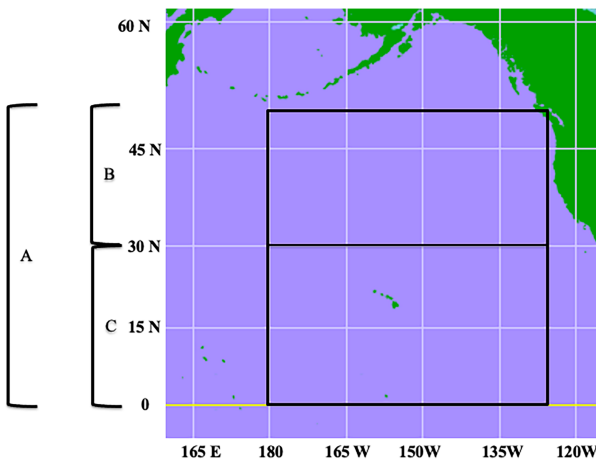


FIG. 1. AOI for the study was a bounding box 50°N, 0°, 125°W, 180° (A). AOI was further divided into two subregions (B) and (C) at 30°N. Base map modified from <https://learningweather.psu.edu/node/59>.

4) TESTING DATASETS

The primary testing dataset for the final three latitude models covered the same AOI and relation to the full moon as the first dataset, but used an independent dataset from December 2019 to November 2020. An additional dataset from 21 May 2020 to 20 July 2020 was used to qualitatively assess the contrast consistency of ML-NVI imagery across the full lunar cycle. Finally, various additional sets were used for qualitative comparisons for specific weather phenomena to include tropical cyclones and fog. The date-time groups (DTGs) for these sets are provided in the case studies.

b. Data processing

First, lunar reflectance values were calculated from DNB radiances using the [Miller and Turner \(2009\)](#) algorithm. VIIRS M-band measurements, [Miller and Turner \(2009\)](#) lunar reflectance values, and DNB radiances were then processed with the Python package Satpy ([Raspaud et al. 2019](#)) to reproject all data to the DNB footprint and corresponding pixels with the nearest neighbor approach. This was done to ensure that the inherent resolution and viewing geometries were consistent. During this process, all data were scrubbed to remove any datasets that had missing values for any of the predictors or predictand. To reduce any additional bias from the bow-tie effect, training and validation datasets were adjusted to only include data in the first aggregated scan of the DNB, specifically to only include 600 pixels to the left and right of nadir. These pixels represent a total distance of 450 km across the scene. This created 25 sets of 90+ matching DTGs, 12 sets for the training and validation datasets and 13 sets for the independent testing dataset. These data could be further divided by month, meteorological season, or latitude if desired.

c. Predictand and predictor selection

To best create and evaluate the ML-NVI model, the resulting predictand must be able to be qualitatively and quantitatively

TABLE 1. List of model predictors, the associated central wavelengths or central wavelength BTDS, and corresponding sensor wavelength range.

| VIIRS band | Central wavelength (μm)/(BTDS) | Wavelength range (μm) |
|------------|-----------------------------------|--------------------------|
| M13 | 4.05 | 3.97–4.13 |
| M14 | 8.55 | 8.4–8.7 |
| M15 | 10.76 | 10.26–11.26 |
| M16 | 12.01 | 11.54–12.49 |
| M13M14 BTD | 4.05–8.55 | — |
| M13M15 BTD | 4.05–10.76 | — |
| M13M16 BTD | 4.05–12.01 | — |
| M14M15 BTD | 8.55–10.76 | — |
| M14M16 BTD | 8.55–12.01 | — |
| M15M16 BTD | 10.76–12.01 | — |

compared to truth. The only nighttime visible data come from the DNB radiances. While scaling of radiances makes visually appealing imagery to the end user, there is no single standard scaling metric or measurement; thus, “quantitative assessments on nighttime visible imagery are challenging given the qualitative nature of most image products, and details of the scenes used for assessments ([Seaman and Miller 2015](#)).” A quantitative assessment of these scaling applications of radiances for digital display would be an assessment of recreating a specific scaling, not against a measured quantity. The [Miller and Turner \(2009\)](#) lunar reflectance is currently the only DNB-derived value that can be used for quantitative comparisons for nighttime data from satellite retrievals. It allows for a quantitative evaluation of model-generated values used for nighttime imagery that has previously been described only for daytime visible imagery or nighttime IR.

The model predictors and associated wavelengths are seen in [Table 1](#). Initial channel selection was based on wavelengths with similar bands between the VIIRS and Advanced Baseline Imager (ABI) sensors. The maximum and minimum values for each wavelength to be used for normalization were taken from the JPSS VIIRS SDR Radiometric Calibration ATBD ([Line et al. 2018](#)). The BTDS selected were based on wavelength relationships highlighted in previous sections. Considerations for channel combinations included all four of [Hillger's \(2008\)](#) recommendations for satellite product development. While experiments were conducted to replicate the current retrieval with fewer predictors, to include not using the BTDS with the understanding that the model would resolve BTDS relationships, these models did not produce the same quality imagery as the all-channel all BTDS retrieval. All predictors were therefore kept. The final input set for training at the largest AOI data consisted of a 2D array sized $510\,394\,368 \times 10$ representing the number of pixels and number of predictors for data in the prescribed AOI and moon criteria. The independent VIIRS assessment 2D array was sized $543\,686\,656 \times 10$.

4. Model architecture and training

We trained a feed-forward neural network (FNN) model to create the ML-NVI from IR BT and BTDS using the dataset

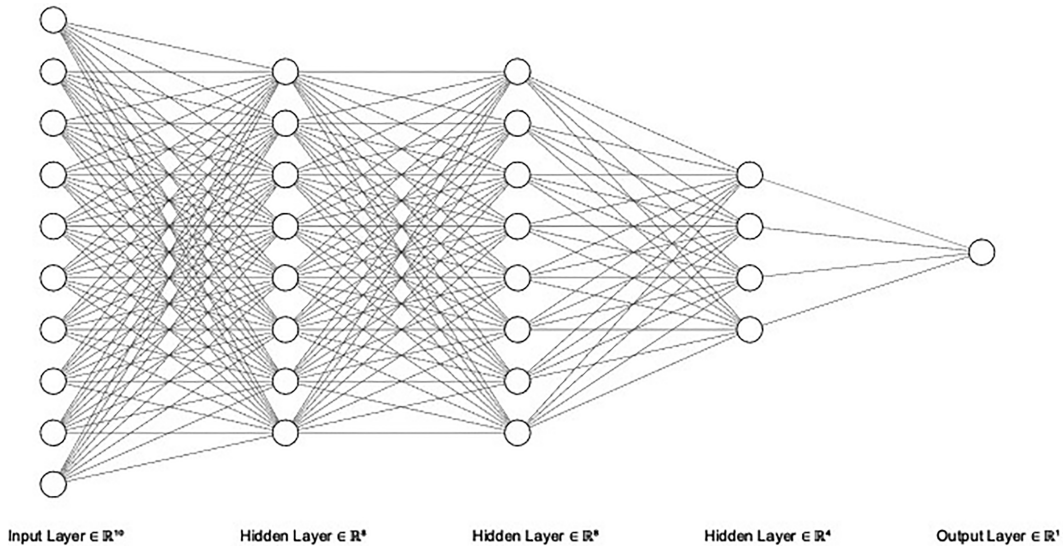


FIG. 2. Architecture for the ML-NVI. Model architecture consists of 10 inputs, 2 hidden layers with 8 nodes, 1 hidden layer with 4 nodes; all with an Adam optimizer, MSE loss function, and ReLU activation functions; and a single node output layer using the sigmoid activation function.

for December 2018–November 2019. The FNN accounts for nonlinearity and processes data pixel by pixel which enables us to further restrict the training dataset more easily if needed. As seen in Fig. 2, the final baseline FNN model has 10 inputs and is composed of three hidden layers (the first two with eight nodes and the third one with four nodes) using rectified linear unit (ReLU) activation and a single node for an output layer that uses sigmoid activation. The model uses an Adam optimizer value of 0.001 and mean-square error (MSE) for its loss function. The number of hidden layers and nodes was chosen after sample runs indicated there was no significant increase to the learning done with further increase in the number of hidden layers or nodes.

Once the baseline model architecture was established, training data were then split 80–20 using the “train_test_split”

function from the Python model sklearn to accomplish model training (Pedregosa et al. 2011). This baseline model was run repeatedly over various batch sizes and epochs for the three different AOIs. Results of this can be seen in Table 2. It was noted that regardless of batch size and latitude data input, training leveled off after 5–10 epochs and then again around 20–30 epochs. The value gained by these extra epochs was minimal in comparison with the values gained in batch size trade-offs. The metric results between varying the batch sizes between 256, 512, 1024, 2048, and 4096 demonstrated that the value gained from smaller batch sizes was minimal in relation to the additional training time. An epoch size of 40 and a batch size of 2048 were chosen for the final model setup. Once the batch and epoch sizes were finalized, training datasets from each latitude range [0°–30°N (tropic model),

TABLE 2. The FNN was trained over various epochs and batch sizes for each latitude to determine the preferred combination based on the training and validation MSE and MAE. The model that had 40 epochs and a batch size of 2048 performed the best overall and most consistently regardless of the latitudes associated with the training data.

| Model (epoch/batch size) | Training latitude | MSE | MAE | V-MSE | V-MAE |
|--------------------------|-------------------|---------|--------|---------|--------|
| 10, 256 | 0°–50°N | 0.0175 | 0.0872 | 0.0179 | 0.0867 |
| | 30°–50°N | 0.0285 | 0.1212 | 0.0287 | 0.1223 |
| | 0°–30°N | — | — | — | — |
| 30, 512 | 0°–50°N | 0.0204 | 0.0988 | 0.0203 | 0.098 |
| | 30°–50°N | 0.02828 | 0.1206 | 0.028 | 0.1202 |
| | 0°–30°N | 0.0083 | 0.065 | 0.00826 | 0.0605 |
| 30, 2048 | 0°–50°N | 0.0178 | 0.0884 | 0.0177 | 0.0884 |
| | 30°–50°N | 0.0289 | 0.1219 | 0.029 | 0.1251 |
| | 0°–30°N | 0.0086 | 0.062 | 0.0086 | 0.0625 |
| 40, 2048 | 0°–50°N | 0.0174 | 0.0868 | 0.0175 | 0.087 |
| | 30°–50°N | 0.294 | 0.125 | 0.029 | 0.125 |
| | 0°–30°N | 0.00847 | 0.0613 | 0.00848 | 0.0622 |
| 30, 4096 | 0°–50°N | 0.0197 | 0.094 | 0.0198 | 0.094 |
| | 30°–50°N | — | — | — | — |
| | 0°–30°N | — | — | — | — |

30° – 50° N (midlatitude model), and 0° – 50° N (full-latitude model)] were processed to create a separate latitudinal model for each region (A, B, and C). All three latitude models were assessed for their skill over all three latitude regions. The division in training and assessment by latitude enabled an evaluation of the differences in training and model evaluation over tropical versus midlatitude SSTs, atmospheric profiles, and cloud features. Furthermore, it helped capture instances where equivalent lunar reflectances can be the same but are indicative of different features. This latitude division also aimed to evaluate the benefit, if any, for latitude-trained specific models versus a global use model.

5. Model evaluation and results

[Loew et al. \(2017\)](#) stated that “the ultimate goal of a validation exercise is to assess whether a dataset is compliant with predefined benchmarks (requirements) that quantify whether a dataset is suitable for a particular purpose.” While requirements for the accuracy of radiometers exist and there are desired skill scores for various radiance-derived products, there are currently no predefined benchmarks for imagery evaluation. The closest benchmark would be the imagery and validation efforts and analysis methods from NOAA–NASA for the ABI channels. This process first conducts visual inspection for feature determination and temporal image consistency. Next, a qualitative comparison with imagery between legacy and current GOES imagery as well as imagery from polar orbiters is done to assure channels are at least a similar quality. Afterward, a quantitative comparison of reflectance and brightness values from level-1B radiances and ground calculated values is done ([Pitts and Seybold 2010](#)). Much of the ABI validation efforts are subjective in their feature determination and comparison of quality to other similar products.

The predefined benchmarks for VIIRS imagery are also qualitative and subjective in nature. As highlighted by [Hillger et al. \(2016\)](#), “A major component in the overall strategy for the Imagery calibration and validation (Cal/Val) effort for the Visible Infrared Imaging Radiometer Suite (VIIRS) is to ensure that the Imagery is of suitable quality for effective operational use. Imagery of sufficient quality is often determined by the ability of human users to easily locate and discriminate atmospheric and ground features of interest.” This demonstrates the highly subjective nature of imagery validation and benchmarks. One user may need a product to highlight upper-level clouds, another may need low cloud features, and a third may need clear free line of sight to the surface. All may look at the same product and come to different conclusions on its usefulness. [Kidder et al. \(2000\)](#) highlighted that satellite-derived products and algorithms need to provide an accurate analysis of the important meteorological features and “do not need to work on the unimportant features of the image.” As an example, they further explained that “an algorithm designed to monitor a low-level feature such as fog/stratus does not need to be precise for high cold clouds.”

The purpose of the study is to create a quantifiable value that represents a physical quantity (pseudo-lunar reflectance) and enables resulting imagery that presents clouds at night

similar to that of visible or DNB imagery. The greatest focus on cloud detection is for low clouds that are otherwise difficult to detect at night; however, the product will be qualitatively compared for the cloud types present in the imagery. Quantitative assessments are done for values across the entire scene and ranges to determine the overall performance of the synthetic lunar reflectance as a substitute for full moon DNB lunar reflectance values. Independent data from December 2019 to November 2020 was used to evaluate all three latitude models in all three AOIs (A, B, and C), resulting in nine sets of statistics and qualitative imagery comparisons.

Similar to [Pitts and Seybold \(2010\)](#), we first conduct a qualitative analysis of imagery from the three latitudinal models in comparison with the Miller–Turner lunar reflectance, IR, and low cloud split window (10.6 – $4.05\text{ }\mu\text{m}$) products to determine the preferred model based on visualization of various cloud features. All three models were compared for the entire dataset, as well as for specific cases, and thus, discussion on these may be included for cloud feature assessment. However, intermodel comparisons will be demonstrated for only a few samples with lunar reflectance range comparisons, lunar cycle assessment, and case studies focused on the latitudinal model of choice. Additional imagery for more comparisons between the three latitudinal models is available upon request.

a. Intermodel comparisons

1) QUALITATIVE ASSESSMENT

The first comparisons, seen in [Figs. 3 and 4](#), are done between DNB lunar reflectance, one VIIRS IR M band, M13 ($4.05\text{ }\mu\text{m}$), the split window (10.76 – $4.05\text{ }\mu\text{m}$), and the three latitude ML-NVI models at the full moon. [Figure 5](#) also provides a sample of all three latitude models but includes M15 ($12.01\text{ }\mu\text{m}$) instead of the split window. The focus for the imagery is for use over open ocean and coastal regions; however, the case samples do include some land features and clouds over land. Each latitude model addresses similar cloud types differently because the models were only trained on data (background SSTs and cloud types) specific to that region. The impact of latitude-specific trained models and their usefulness for other regions is most apparent in the top-left corner of [Fig. 4](#) where the tropical model has created additional cloud cover over the clear ocean due to the SSTs. The contrast is apparent in the overall contrasts between the three models in [Figs. 4–6](#). The added contrast provides the ability to gain more depth of clouds in the ML-NVI over the other IR channels and products. This demonstrates the potential to catch a forecasters’ eye more easily when they are reviewing imagery and make a better assessment of the cloud features in question.

Beginning with existing products, [Fig. 3](#) highlights differences between the DNB lunar reflectance, M13, and the split window (10.76 – $4.05\text{ }\mu\text{m}$) in how each addresses the ship tracks that are centered on 39° N and 123° W. While present in all imagery except the shortwave infrared (SWIR), their signal is strongest in the lunar reflectance, the midlatitude ML-NVI, and the full-range ML-NVI.

Qualitative ML-NVI Model Comparisons

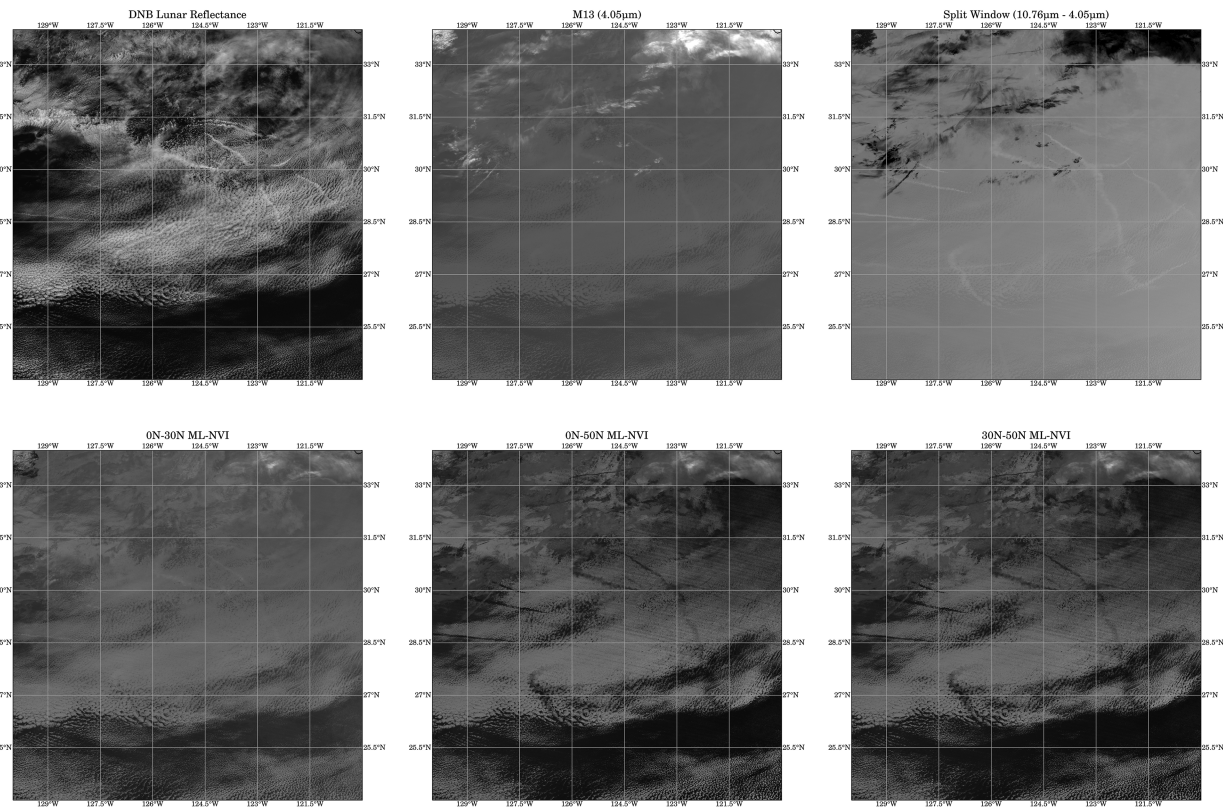


FIG. 3. (top) Qualitative comparisons (left to right) of images from DNB radiance calculated lunar reflectance, VIIRS M13 (4.05 μm), and VIIRS SW (10.76–12.01 μm) sensors and (bottom) predicted lunar reflectance for the three latitudinal models (full latitude, tropical latitudes, and midlatitudes). Image is from the northern Pacific open ocean at 1026 UTC 12 Dec 2019.

The model trained on data from 0° to 30°N has the least contrast of the three models over these samples. This is because the observed BTs in the predictors are much colder than the tropical SSTs that represented clear skies so the model assumes that there must be interference to the surface and the BT interpretation is a reflectance indicative of a constant thin cloud layer over cold SSTs. This results in lunar reflectance values that are in a smaller range and overforecast reflectance values for clear skies. This model did have decent contrast and performance in the tropical cyclone (TC) examples and scenes over warm SSTs. This demonstrates that this model will only perform well with warm background SSTs. The model trained from 30° to 50°N appears to have the greatest contrast of the three models and may be the closest to the DNB at first glance. This is because these images cover a majority of the latitudes that this model was trained on.

Thin cirrus is absent in the DNB, appears bright white in the IR blocking the underlying clouds, and appears as a semi-transparent mask that you can “see through” to the clouds beneath in the three ML-NVI models. Due to its transparency, we can still detect low to mid-clouds in layers below it that are absent or blocked in the IR imagery.

Additionally, all three latitude models capture low-level clouds, such as open ocean stratocumulus, that are visible in

the DNB lunar reflectance but not captured well, if at all, in the IR samples as seen in the bottom of all images in Fig. 3, with the best contrast in the full-latitude model. Though not as bright as DNB lunar reflectance, it is possible to infer the layers of clouds in the models similar to the DNB with higher/thicker clouds being brighter (colder) in comparison with lower and with more contrast for lower-level features than seen in the IR. This assessment holds true with the exception of the previously mentioned cirrus clouds that are optically thin and appear translucent but darker than thick cumulus. Through additional imagery assessments, it was determined that although the contrast varies between the three latitude models, all models are able to capture ship tracks and provide better texture of clouds to help indicate actual cloud feature versus a uniform field as seen in IR. Figure 5 is used to highlight the differences in model performance over warmer SSTs found in tropical regions and demonstrates its capabilities and limitations with convective activity. In this case, the midlatitude model captures in the lower-right corner the best; however, it struggles with contrast for the lower-level cloud features in the tropics just like the tropical model did at midlatitudes.

In comparison with the single-channel IR wavelength imagery, the human eye can visualize the low-level cloud features

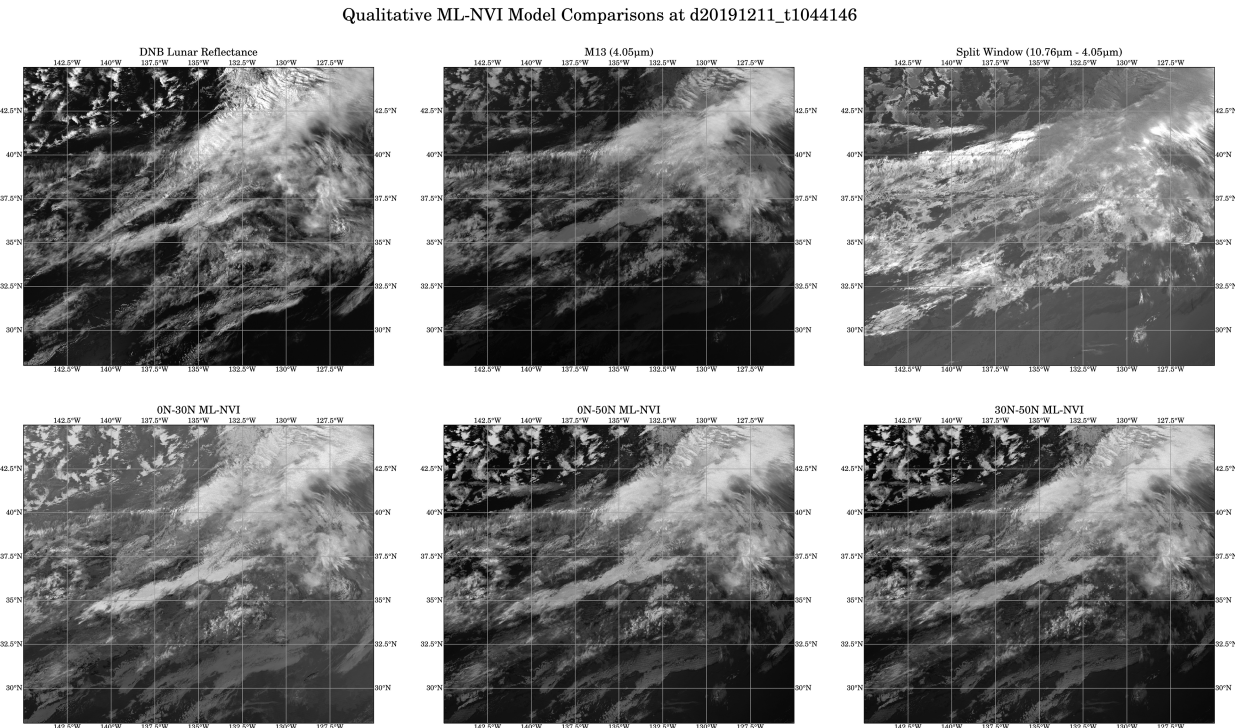


FIG. 4. (top) Qualitative comparisons (left to right) of images from DNB radiance calculated lunar reflectance, VIIRS M13 ($4.05\text{ }\mu\text{m}$), and VIIRS SW ($10.76\text{--}4.05\text{ }\mu\text{m}$) sensors and (bottom) predicted lunar reflectance for the three latitudinal models (full latitudes, tropical latitudes, and midlatitudes). Image is from the northern Pacific of the West Coast of the United States and over open ocean at 1044 UTC 11 Dec 2019.

better in the models. As model predictions are created from thermal emissions, the contrast between clear skies and clouds does not appear as vividly as the true DNB lunar reflectance. The clouds appear brighter than the clear skies, and intuition would show low and layered clouds, missed by IR interpretation alone, are present. An additional example of texture and this contextual clue to forecasters is in the lower-right corner of Fig. 4 in which all models capture clouds similar to the DNB lunar reflectance, while the texture is minimum in the IR and split window. The models are also able to remove man-made lights seen in Fig. 10 most likely due to the lights not having a signature in the IR channels as they do in the visible. In the absence of city lights, populated areas appear darker (warmer) than the surrounding land which may be capturing the presence of urban heat islands. More investigation must be done before determining the performance of the ML-NVI for clouds over land.

Qualitatively, the full-latitude model performed best for all the cloud types and accounts for all SSTs between 0° and 50°N that are seen in open oceans, appearing similar to the low-latitude model in the tropics and to the midlatitude model in the middle latitudes.

2) QUANTITATIVE ASSESSMENT

An evaluation of the underlying data distribution for each model is done before evaluating the specific sets of observational points. Comparisons of the distribution of the three

latitude model predictions for the validation sets relative to each other and the true reflectance can be seen in Fig. 6. Note that the lunar reflectance value distribution is not normally distributed. The probability density functions (PDFs) further not only highlight the percent of observation types (i.e., reflectance values) but also visually demonstrate differences in cloud detection ability at various reflectance values and by models. A difference in the value density when compared to the DNB distribution is most present in areas of low reflectance and is common for all three models. As noted in the qualitative assessment, this shift is partly due to the capturing of cirrus clouds by the ML-NVI. All three models appear to have performed similarly in this shift and throughout the range of reflectances in the PDF; however, visually we see how the specific model differences manifest when turned into imagery. From approximately $0.1\text{--}0.35$ reflectance values, the low-latitude model underforecasted values, while the midlatitude model overforecasted values, and above 0.35 , the inverse is true. The middle reflectance values are the hardest to detect and may be indicative of layered clouds, low or midlevel clouds, or scenes where the cloud features are smaller than satellite pixels. The full-latitude model appears to perform best in these cases. The highest reflectances represent optically thick clouds and thunderstorm clouds that are typically well identified in the IR due to the strong thermal contrast. A cursory look of the PDFs indicates that the full-latitude model has the greatest distribution similarity to the truth across the

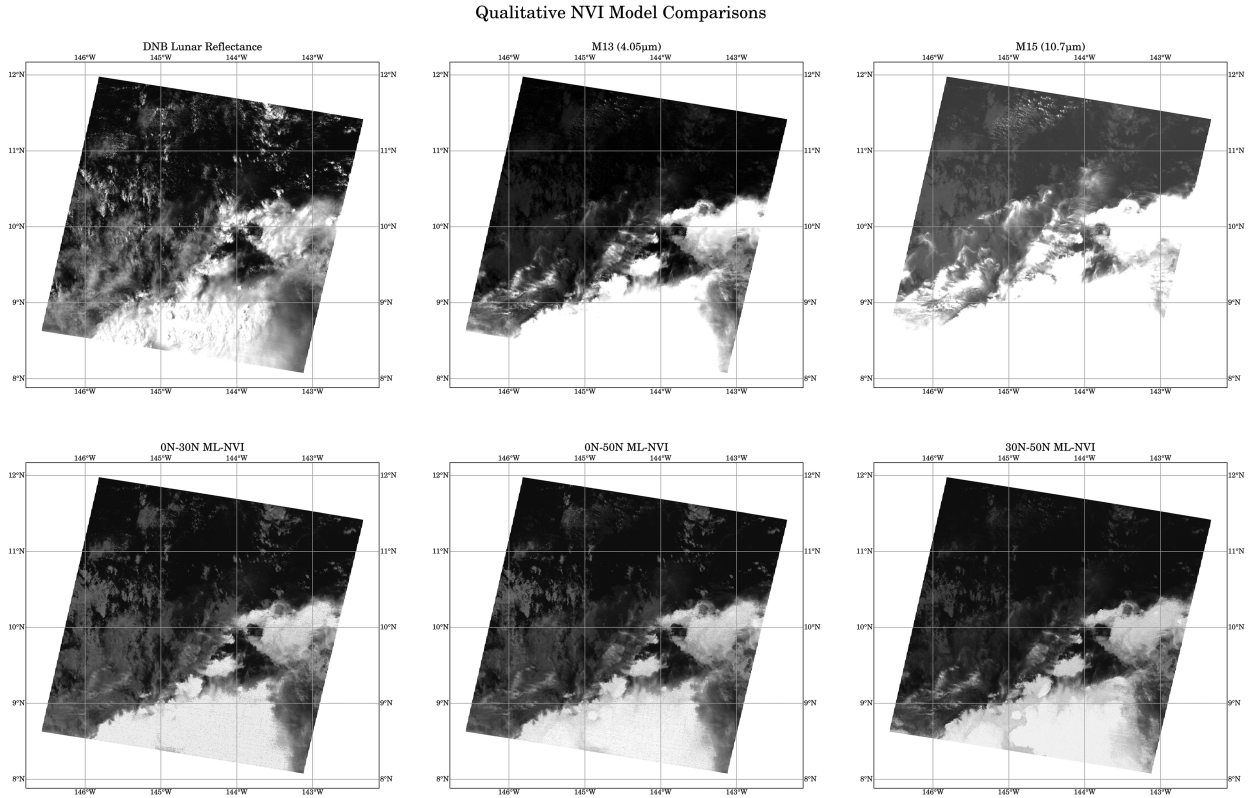


FIG. 5. (top) Qualitative comparisons (left to right) of images from DNB radiance calculated lunar reflectance, VIIRS M13 (4.05 μm), and VIIRS SW (10.76–4.05 μm) sensors and (bottom) predicted lunar reflectance for the three latitudinal models (full latitudes, tropical latitudes, and midlatitudes). Image is from the northern Pacific at lower latitudes over open ocean between Mexico and Hawaii at 1113 UTC 12 Dec 2019.

reflectance spectrum. Important to note in the PDF is the location of the spikes in the larger lunar reflectance values seen across all datasets. It peaks at 1 in the lunar reflectance as this is a maximum set as reflectance, in theory, would not extend beyond this. However, due to scattering, signal noise, and city lights, measurements may exceed 1. Underforecasting trends and biases can be seen in the models based on the location of this peak and can give insight into the range of values each model may predict.

Next, statistical calculations were conducted to assess the overall capability of the ML-NVI for full moon scenes over the open ocean for all three models at all three latitude ranges. The product is designed to function regardless of moon phase; however, model creation and quantitative validation were conducted near the full moon, as this is when the highest quality DNB data are available.

During visual inspection of the qualitative imagery, it was observed that sections of the lunar reflectance imagery patches were fully black although there were no missing data in the raw DNB radiances. It was determined that this was due to the specific moon angles for which the [Miller and Turner \(2009\)](#) lunar reflectance is not calculated; thus, all data points where the DNB lunar reflectance truth was either 0 or Not a Number (NAN) were removed. These points account for approximately 2% of the evaluation data and, while

present for imagery creation, were removed before statistical calculations were performed and PDF distributions were created.

Quantitative scores for the three models are provided for the overall datasets, and thus, there is unintentional weighting based on the reflectance distribution. A chart of the statistical results for all three latitudinal model assessments at the three validation latitudinal bands is provided in [Table 3](#). There are currently no other published data utilizing lunar reflectance to provide baseline metrics for direct comparisons. As nighttime visible data become available, it will be critical to ensure comparison metrics are made between similar datasets. For this reason, metrics are based on all valid pixels and are not currently divided by cloud type or height.

The three models were compared using the following metrics: explained variance, R^2 -squared, root-mean-square error (RMSE), mean absolute error (MAE), Spearman's correlation, correlation coefficient (CC), Kullback–Leibler divergence (KLD), and Jensen–Shannon divergence (JSD). As expected, performance metrics were generally best when individual latitude models are evaluated on the same latitude ranges they were trained on. Still, there was only a 12% difference in the explained variances between the best and worst models for a latitude. When looking at overall error, lunar reflectance was evaluated from 0 to 100 and the differences

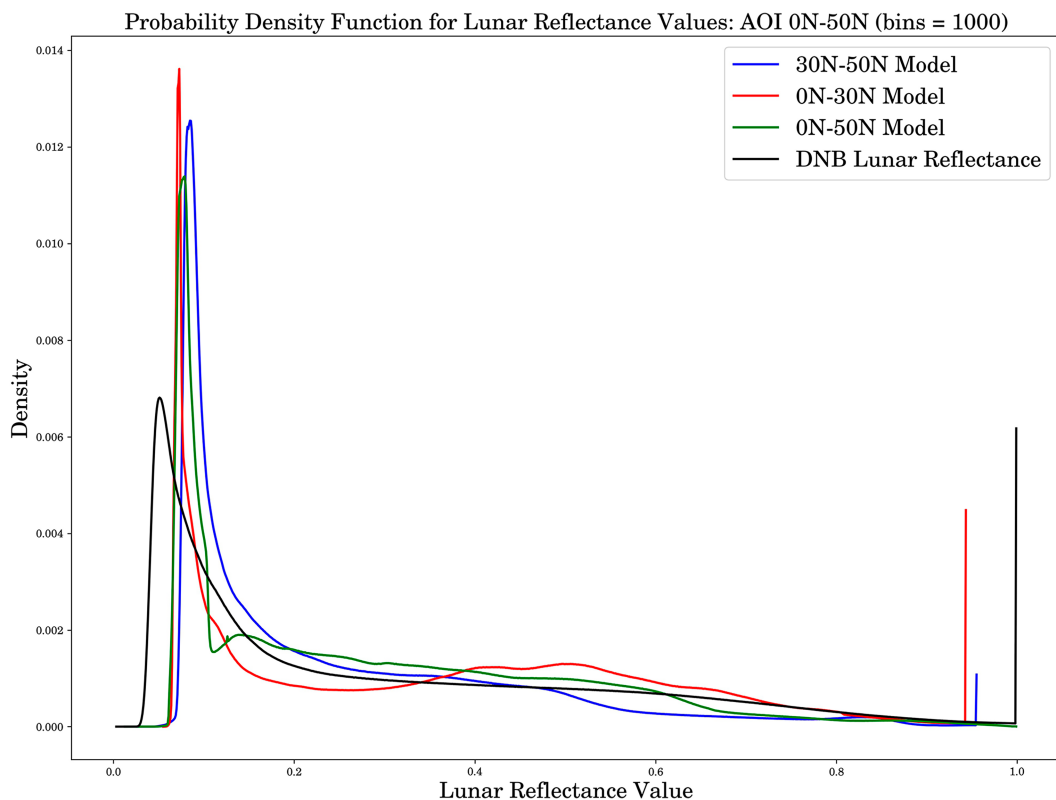


FIG. 6. PDFs of the three latitudinal model lunar reflectance distributions vs the true DNB lunar reflectance distribution for the 0° – 50° N validation AOI.

ranged between 3 and 4 for MAE with the exception of the tropical model performance over midlatitude ranges which was significantly worse than the midlatitude and full-latitude models for this area. It is important to note that the model performance on the full-latitude dataset may also be biased toward the percentage of data points made up by each latitude range.

Using the full set of predictors, the model has an explained variance value of 0.76. While this is a good value, especially as it only considers spectral relationships, the inclusion of a

predictor with information on spatial context may further improve skills in model variance. The ranges of MAE and RMSE further demonstrate the spread of the data and are within a reasonable amount when considering that lunar reflectance is a visual proxy for total cloud cover which is often measured in octas. Spearman's correlation and correlation coefficients between the ML-NVI and true DNB lunar reflectance range between 82% and 89%, indicating a strong positive relationship between the two. To further quantify this relationship, KLD and JSD scores were calculated. JSD

TABLE 3. A consolidation of the validation metrics for all three latitude models across all three latitude validation regions. Scores for the full-latitude model in the 0° – 50° N AOI demonstrate model performance for the use of a singular global model across all seasons and latitude.

| 2020 ML-NVI validation metrics | | | | | | | | | |
|--------------------------------|----------------|--------------------|-------|-------|-------|----------------------|------|------|------|
| Model | Latitude range | Explained variance | R2 | RMSE | MAE | Spearman correlation | CC | KLD | JSD |
| 0°–50°N full latitude | 0°–50°N | 0.76 | 0.76 | 11.83 | 8.2 | 0.86 | 0.87 | 0.08 | 0.14 |
| | 30°–50°N | 0.67 | 0.67 | 14.42 | 11.34 | 0.82 | 0.82 | 0.08 | 0.15 |
| | 0°–30°N | 0.8 | 0.79 | 10.20 | 6.35 | 0.87 | 0.9 | 0.07 | 0.13 |
| 30°–50°N middle latitude | 0°–50°N | 0.72 | 0.682 | 13.56 | 9.0 | 0.85 | 0.85 | 0.09 | 0.15 |
| | 30°–50°N | 0.68 | 0.657 | 14.63 | 10.99 | 0.83 | 0.83 | 0.08 | 0.14 |
| | 0°–30°N | 0.71 | 0.655 | 13.19 | 7.98 | 0.85 | 0.85 | 0.1 | 0.15 |
| 0°–30°N low latitude | 0°–50°N | 0.64 | 0.577 | 15.68 | 10.77 | 0.8 | 0.81 | 0.11 | 0.17 |
| | 30°–50°N | 0.51 | 0.166 | 22.85 | 18.24 | 0.71 | 0.72 | 0.13 | 0.19 |
| | 0°–30°N | 0.83 | 0.83 | 9.33 | 6.23 | 0.87 | 0.91 | 0.06 | 0.12 |

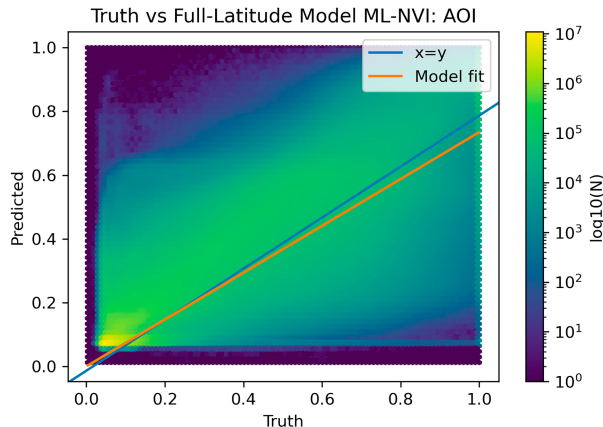


FIG. 7. Data comparison of the 2020 validation data and the true DNB lunar reflectance for the full-latitude model over the 0°–50°N AOI.

scores range between 0 and 1 with the lower number indicating the similarity or minimal divergence between the two sets. The JSD scores for the full-latitude model ranged between 0.12 and 0.15 and indicate there would be only a small adverse impact if the ML-NVI values were to be used in place of the DNB lunar reflectance for modeling or calculations if using the full-latitude model to create lunar reflectance and these are only 0.01 higher than the scores obtained by the sublatitudinal models as demonstrated in Fig. 7 with the full lunar cycle. This highlights the ability to have a greater visibly intuitive product with a scaled consistency for forecasters across the lunar cycle as the ML-NVI predicts what a full moon lunar reflectance would be regardless of the actual moon phase, angle, and existing lunar reflectance and the ability to use one model (full latitude) for the whole globe. It is possible to infer what lunar reflectances would be expected for the observed phenomena at any lunar phase if a full moon existed instead based on the lunar reflectance values created from our model. From this, it could be possible to even utilize daytime cloud mask algorithms at night if the day and night reflectance differences in the 3.9- μm band are accounted for (Miller et al. 2022).

3) MODEL OF CHOICE

Based on qualitative analysis over imagery in the AOI covering all full moon periods from December 2019 to November 2020, and model prediction metrics, the full-latitude model (0°–50°N) is the best-performing model overall. For midlatitudes, it holds its own against the 30°–50°N (midlatitude) model and significantly outperforms the 0°–30°N (tropical) model. In the tropical regions with warmer SSTs, it is very similar in model performance to the tropical model, while the midlatitude model has the poorest performance. Quantitatively, the full-latitude model reflectance values are the most closely aligned to the DNB reflectance and provided the best representation of clouds among the three models with minimal loss of information. Because of this, the full-latitude model is the model of choice, and the remainder of model

validation and future case studies will be on the full-latitude model, hereby referred to as the ML-NVI.

b. Model of choice performance

1) LUNAR REFLECTANCE RANGE ASSESSMENT

Overall model performance was addressed during intermodel comparisons, but an assessment of the chosen model's performance over ranges of reflectance values is also useful. In addition to the previously discussed PDF in Fig. 6, a scatterplot of the full-latitude model's performance versus the true DNB lunar reflectance can be seen in Fig. 7. The lower-left corner represents clear skies with lunar reflection values in truth and predictions of zero, and the upper-right represents lunar reflectivity values of one in each. The one-to-one line and model best-fit lines are also noted. The scatterplot shows a positive trend between the datasets, and though in some lunar reflectance value ranges they appear to be much more widely distributed along the one-to-one line, the relative differences in the dataset are small.

Because of data distribution and interest in performance over specific data ranges, we look to assess differences in lunar reflectance values between the truth and model at multiple lunar reflectance ranges. The World Meteorological Organization (WMO) suggests that for cloud cover comparisons, data and models/predictions be divided into cloud categories versus a continuous scale, though they do not specify category thresholds (Zhongming et al. 2012). WMO height and total cloud cover categories for observations and terminal aerodrome forecasts usually line up with aviation flight safety requirements (Weiss 2001). A review of research shows that most studies divide the total cloud cover into observational categories based on sky octa obscuration (clear, few, broken, scattered, and overcast), into three categories based on cloud amount (clear, partly cloudy, cloudy), or into 10% bins for precise measurements of cloudiness (Warren et al. 1988; Kidder and Vonder Haar 1995; Hogan et al. 2009; Zhongming et al. 2012). When using satellite, threshold techniques are a common way to delineate between cloud amount categories and transfer well for reflectance values (Kidder and Vonder Haar 1995). Solar reflectance values for clear skies over the open ocean range between 0 and 0.2; thus, these values would represent clear skies in lunar reflectance as well, while pixels with values above that would have some form of clouds (Ackerman et al. 1998; Kim et al. 2017).

Data were divided into five even ranges of true lunar reflectance values (0–0.2, 0.2, 0.4, 0.4–0.6, 0.6–0.8, and 0.8–1), and value differences between the truth observed lunar reflectance values and full-latitude model predicted lunar reflectance values as well as the mean and standard deviations are seen in Fig. 8 for the five subranges. The percentage of the overall data based on bin ranges is shown in Table 4. Considering this breakout, and referencing Fig. 6, a large amount of the dataset included clear skies; thus, the overall dataset standard deviations may be biased toward the model performance on the lower lunar reflectance values.

Dividing the dataset into these ranges of lunar reflectance versus looking solely at the overall dataset deviations enables

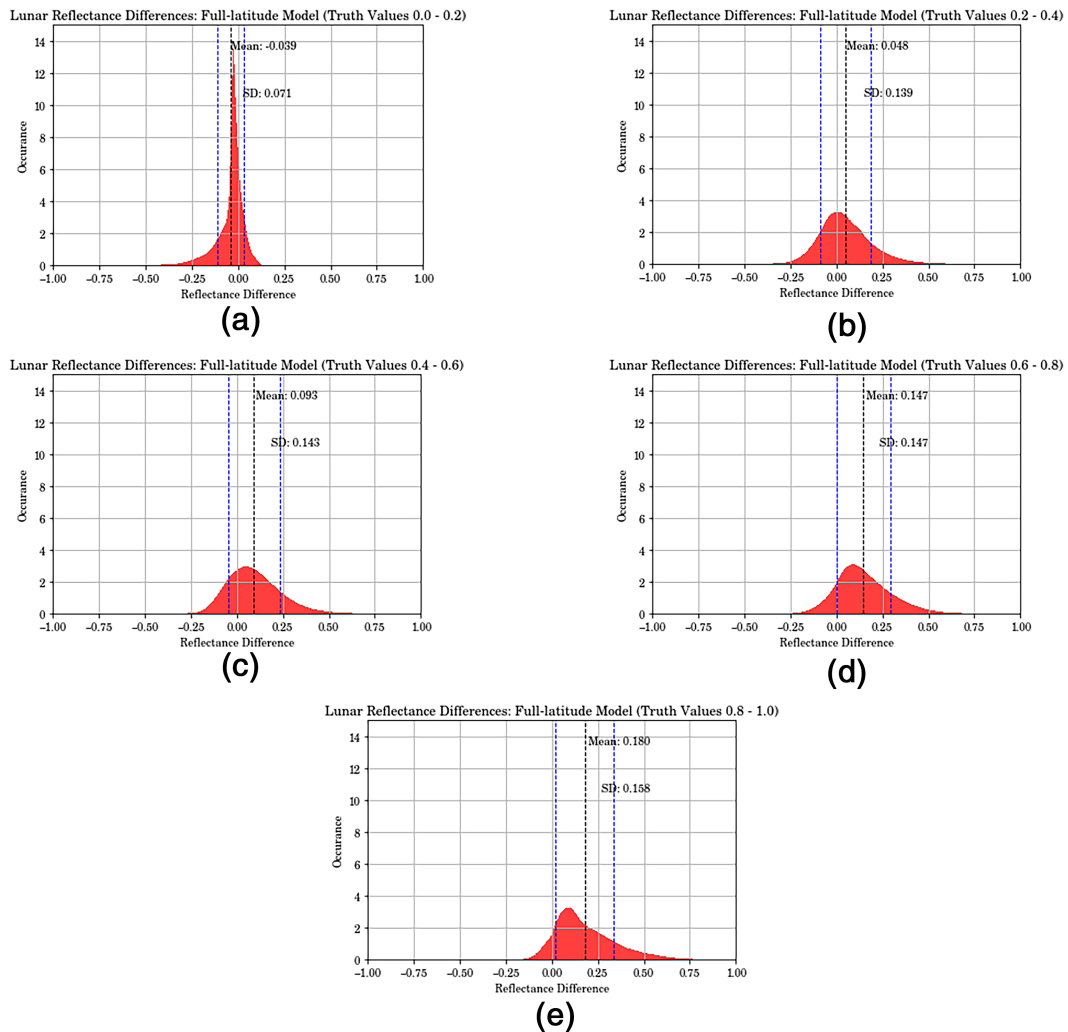


FIG. 8. Distribution of true DNB lunar reflectance—full-latitude model reflectance differences evaluated at 0°–50°N AOI for true lunar reflectance values between (a) 0.0–0.2, (b) 0.2–0.4, (c) 0.4–0.6, (d) 0.6–0.8, and (e) 0.8–1.0.

an additional understanding of model performance. Lunar reflectance values less than 20 usually represent clear skies; however, they can also represent the presence of optically thin clouds such as cirrus, which the DNB does not detect but the ML-NVI does as seen in the qualitative imagery assessment, or low stratus. As reflectance values increase, optical depth values also increase, and this could be due to layer

TABLE 4. Dataset composition across five range bins used in evaluating skill for lunar reflectance differences.

| True lunar reflectance value range | Percentage of dataset |
|------------------------------------|-----------------------|
| [0, 0.20] | 50.5 |
| [0.2, 0.4] | 19.9 |
| [0.4, 0.6] | 15.7 |
| [0.6, 0.8] | 10.1 |
| [0.8, 1] | 3.8 |
| [0–1] | 100 |

clouds or growing cumulus. This evaluation is not a direct assessment of how the model performs for various cloud types or cloud heights but does provide insight into performance for different lunar reflectance ranges in which performance can be inferred (Liou 2002; Kidder and Vonder Haar 1995). In general, the larger the values of lunar reflectance, the greater the standard deviation in truth model values. Additionally, at lower values the model tended to predict greater lunar reflectance values more often than in the DNB lunar reflectance, but as the true lunar reflectance values increased it tended to underpredict the reflectance values more and with a greater deviation.

2) LUNAR CYCLE ASSESSMENT

In addition to analysis at full moon, a qualitative assessment was done on ML-NVI performance over the full lunar cycle for the model of choice, the full-latitude model. The DNB sensor gathers radiance values from sources other than the moon (airglow, city lights, aurora, etc.); because of

this, some DNB products (HNCC, NCC, and erf scaling) can create images regardless of the moon phase, but additional processing must be done and imagery is not standardized to retain the same contrast across the lunar cycle. Lunar reflectance cannot be calculated for all phases as the Miller-Turner calculations require the moon to be at a specific lunar zenith angle. [Figure 9](#) makes comparisons between DNB lunar reflectance imagery, the full-latitude model imagery, and M-band 15 (12.01 μm) for two lunar cycles over the Hawaiian Islands, a region of warmer SSTs. During half of the lunar cycle, lunar reflectance data are not able to be calculated; thus, imagery based on reflectance is not available (as seen by the black images for lunar reflectance in [Fig. 9](#) rows 1 and 3) and other DNB-scaled products must be used. The ML-NVI provides lunar reflectance values and visual imagery similar to that of DNB that would appear at full moon periods but with consistent shading across the lunar cycle as seen in the center column of [Fig. 9](#). Since IR is fully emissive and the model was trained solely on full moon scenes, calculated model reflectance values do not respond to lunar cycles and ML-NVI can provide visually consistent nighttime visible imagery, even when DNB lunar reflectance is not available, that enhances cloud identification over IR alone, allowing users to learn only one presentation of features for the full lunar cycle versus varying representations as seen in most DNB enhancements. In comparing the ML-NVI to the IR over the mountains of the Big Island (located in the region bounded by 19°, 20°N, 156° and 155°W), as seen in the second row, the ML-NVI does not interpret these cold land features as clouds with large cold signatures.

6. Case presentation and conclusions

After a general qualitative and quantitative assessment of the ML-NVI's ability to detect cloud and clear skies across the full lunar cycle, ML-NVI was applied to specific meteorological phenomena where the improved detection of low clouds may benefit observers and forecasters. ML-NVI can enhance the detection of low clouds at night over traditional IR, which is especially critical for fog formation and tropical cyclone (TC) forecasting.

a. Fog cases

Enabling a forecaster to better visualize fog formation, extent, and dissipation can enhance flight safety and aid to minimize impacts from fog to busy coastal airports and for mariners at seaports. [Figure 10](#) shows two fog events: The top row is of a coastal fog event on 7 September 2020 with 82% illumination, and the bottom row is an event of Mexico on 6 October 2017 when there was 99% illumination. In addition to coastal fog over California on 7 September 2020, California had a series of wildfires and significant smoke. This can be seen in the lunar reflectance imagery as the city lights appear hazy in the interior regions near where fires were located. More details about these events are found in a recent publication by [Miller et al. \(2022\)](#) which also highlights the importance of reliable nighttime low cloud detection. While both

cases are for periods of high illumination, the case for Mexico is outside of the initial model AOI and both show potential subjective performance over land. A quick look shows overall greater contrast in the clear and cloud portions of the images with the best being in the DNB lunar reflectance, followed by the ML-NVI, the split window, and then traditional IR. When comparing the ML-NVI to the IR or split window, especially noticeable is how clear the extent of the fog bank appears and the texture in the ML-NVI. The ML-NVI also appears to capture to some degree SST differences as seen in the California case. A comparison to the daily SSTs and the extent of the wildfire smoke shows that the turbulent features seen in the ML-NVI imagery along the California coast must be due to the SSTs.

One of the key elements of forecasting fog dissipation is the point of the forecast location with respect to the fog boundary ([Gurka 1978b,a](#)). The ML-NVI provides good ability to detect this boundary as seen in [Fig. 10](#) with the fog boundary for the region in the lower-left corner detectable in DNB and ML-NVI but harder to detect from the IR and split window. From this, one may be able to determine more precisely the extent of the fog layer and time of its dissipation. [Miller et al. \(2022\)](#) highlighted that the bottom case was an event in which the split windows incorrectly identified fog which was then utilized as a cloud mask. It appears that this may be the case for areas along the coast and to the southwest of Mexico looking at the split window versus the DNB and the ML-NVI. An additional potential use of ML-NVI can be to improve cloud masks. We also see the location of the California coastal current, compared to the open ocean in the ML-NVIs due to the significant temperature SST contrast; however, its uniform smooth texture helps to identify it as such versus low clouds for visual analysis especially when combined with the lunar reflectance product. There may be other beneficial uses for visualizing the SST contrast, but they were not explored at this time. On land, we see city lights removed with the ML-NVI. In this case, this enhances the ML-NVI's ability to see the fog inland from the Monterey Bay region at 37°N, 122°W. Overall, the ML-NVI highlights the fog better than the IR or the split window and is helpful for detecting the fog extent when not possible with DNB due to illumination.

b. Tropical cyclone case

The Operational Line Scanner (OLS), the predecessor to the DNB, determined there was a 1–2°/60–120 nautical mile (n mi; 1 n mi = 1.852 km) difference in pinpointing the center position location of tropical cyclones between using IR and nighttime visible sensors for low-level circulation ([Miller et al. 2006](#)). Additionally, the turn to using nighttime visible sensors such as OLS and DNB over IR when available had significant effects on wind fields and forecast timing ([Miller et al. 2006](#)). By using the ML-NVI in the same capacity that OLS or DNB is currently used for both manual and automated processes such as in CIRA's red-green-blue (RGB) multispectral enhancement or the Automated Rotational Center Hurricane Eye Retrieval-II (ARCHER-II) algorithm, center position

Qualitative Comparisons Lunar Cycle

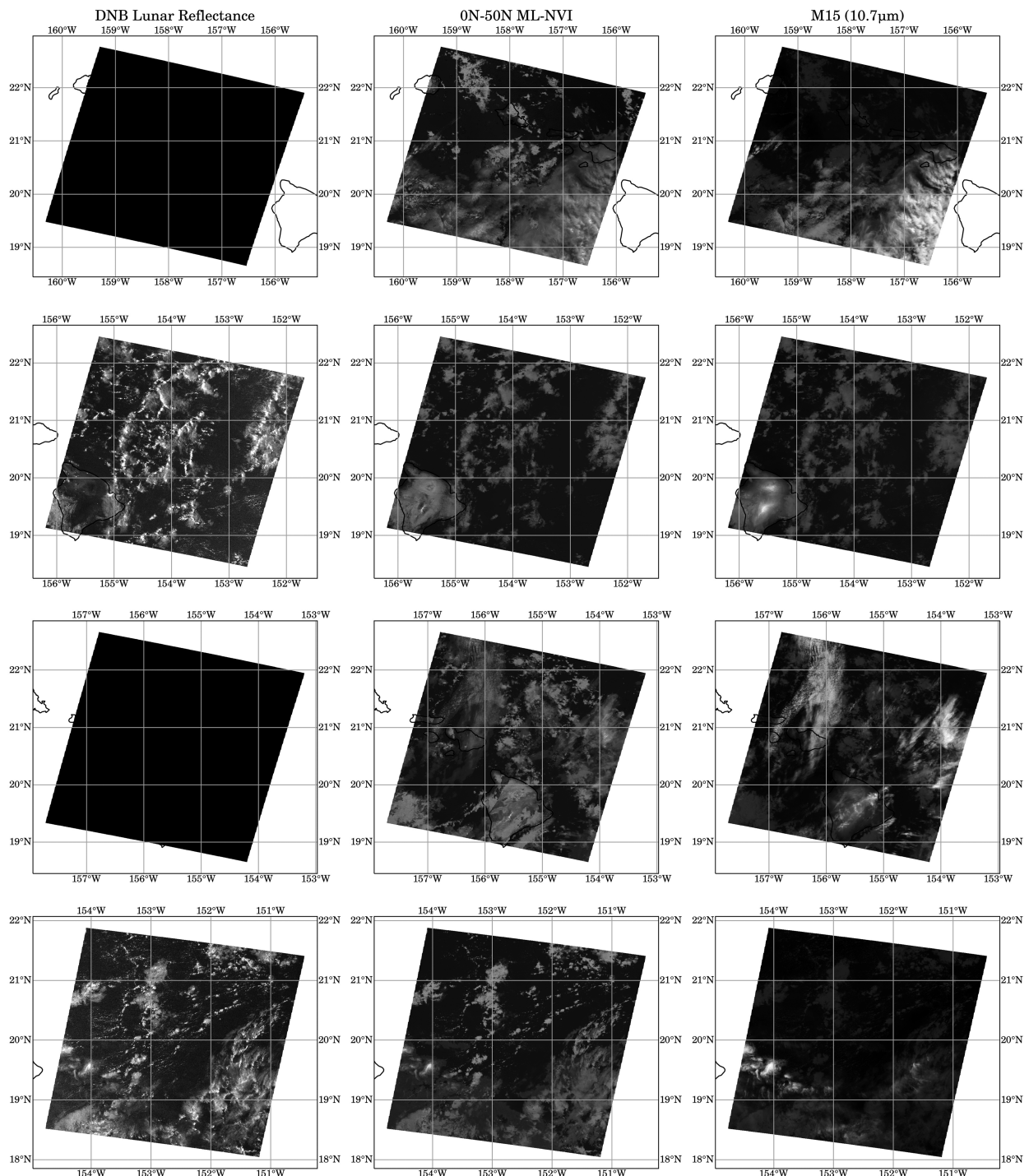


FIG. 9. Lunar cycle comparisons (left to right) of images from DNB lunar reflectance, full-latitudinal model lunar reflectance, and M15 (12.01 μm) for (top to bottom) 1210 UTC 28 May 2020, 1220 UTC 2 Jun 2020, 1222 UTC 23 Jun 2020, and 1128 UTC 12 Jul 2020. High-illumination periods are seen in rows 2 and 4 with low-illumination periods in rows 1 and 3. The quality and contrast of the ML-NVI imagery seen are consistent over the full lunar cycle (center).

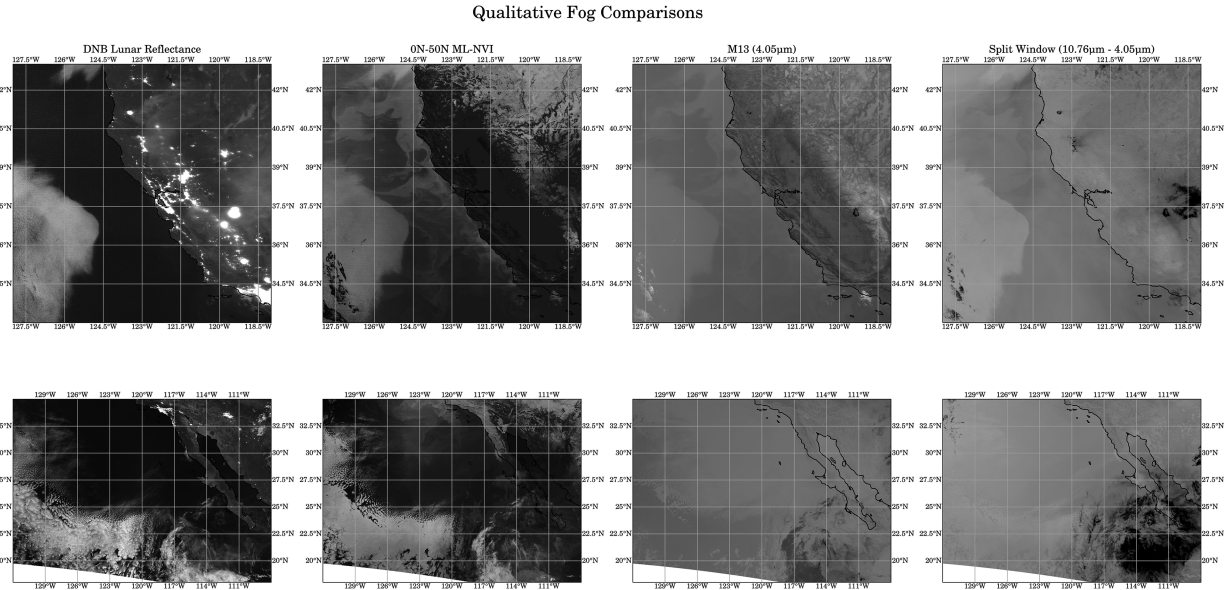


FIG. 10. Qualitative comparisons (left to right) of images from DNB radiance calculated lunar reflectance, VIIRS M13 (4.05 μm), and VIIRS SW (10.76–4.05 μm) sensors and predicted lunar reflectance for the full-latitude model. Images are from the northern Pacific open ocean on (top) 0907 UTC 7 Sep 2020 and (bottom) 0931 UTC 6 Oct 2017.

fixes may become more precise than current nighttime IR fixes as illustrated previously (Wimmers and Velden 2016). Furthermore, animated ML-NVI imagery can help separate the layers of cloud rotation and may improve the determination of TC intensity using Dvorak techniques and structure knowledge in comparison with LWIR animations. Examples of this are highlighted in the image comparison for Typhoon Fengshen in Fig. 11. This cyclone case occurred outside the AOI that was used for model training and validation demonstrating an expanded use of the model.

West Pacific Typhoon Fengshen is seen in Fig. 11. The samples are from 13 November 2019 at 1438 UTC (top row) and 1529 UTC (bottom row), respectively. Lunar illumination for this period was at 99%. Due to the location of the storm, successive satellite passes approximately 50 min apart were able to capture changes in the structure of the system. The DNB lunar reflectance in the second row shows a circulation center around 17°N and 152°E. In the corresponding ML-NVI, there is a dark spot in the lower clouds in the same area, and in the IR, this clearing is not present. Both rows show a long cloud feature oriented from southwest to northeast in the box bounded by 12°, 14°N, 150°, and 153°E. The imagery contrast and structure of this feature are most prominent in the DNB lunar reflectance imagery, but are also apparent in the ML-NVI. This feature is present in the IR, but its shape is obstructed by upper-level cirrus. In this case, the ML-NVI provides a better assessment of storm structure than the IR for use with the Dvorak technique. Additionally, individual areas of convection centered around 18°N and 150°E are noticeable in all three imagery types but appeared to be merged in the IR, while the ML-NVI permits the detection of more individual convective areas presently seen in the corresponding DNB

lunar reflectance. Though these are data from the VIIRS channels, viewing two consecutive passes over the system aids to demonstrate the benefit to TC forecasting that a geostationary DNB-like product may provide even if its resolution is not as refined as the DNB sensor as instead of two images there could be from 5 to 50 depending on which scan is available over the storm.

c. Conclusions

In this study, an ML model was developed using LWIR to create pseudo-DNB lunar reflectances at full moon. Lunar reflectances are derived from measured satellite radiances enabling quantifiable metrics for nighttime synthetic imagery products. Quantitative evaluations of the ML-NVI were conducted with scores as seen in Table 3. Imagery created from the synthetic lunar reflectance provides nighttime imagery to the end user that behaves similar to DNB and solar visible imagery, retains a transparent visualization of upper-level clouds, and still enables the ability to see lower-level clouds unless it is a very dense and optically thick cloud as seen in Figs. 3–5, 7, 10, and 11.

The implications for environmental applications are numerous. First, the ML-NVI provides a product that improves the contrast issues seen in most DNB imagery products and preserves a constant contrast regardless of the lunar cycle. This is more intuitive to a forecaster and does not require additional calculations or lookup tables as may be needed for scaled DNB radiance products. This can aid in forecasting, especially for polar regions, where there is more frequent coverage with the JPSS satellites. Next, as seen above, ML-NVI can enhance the ability to detect fog and low-level tropical circulations more easily than IR alone or the low cloud split window

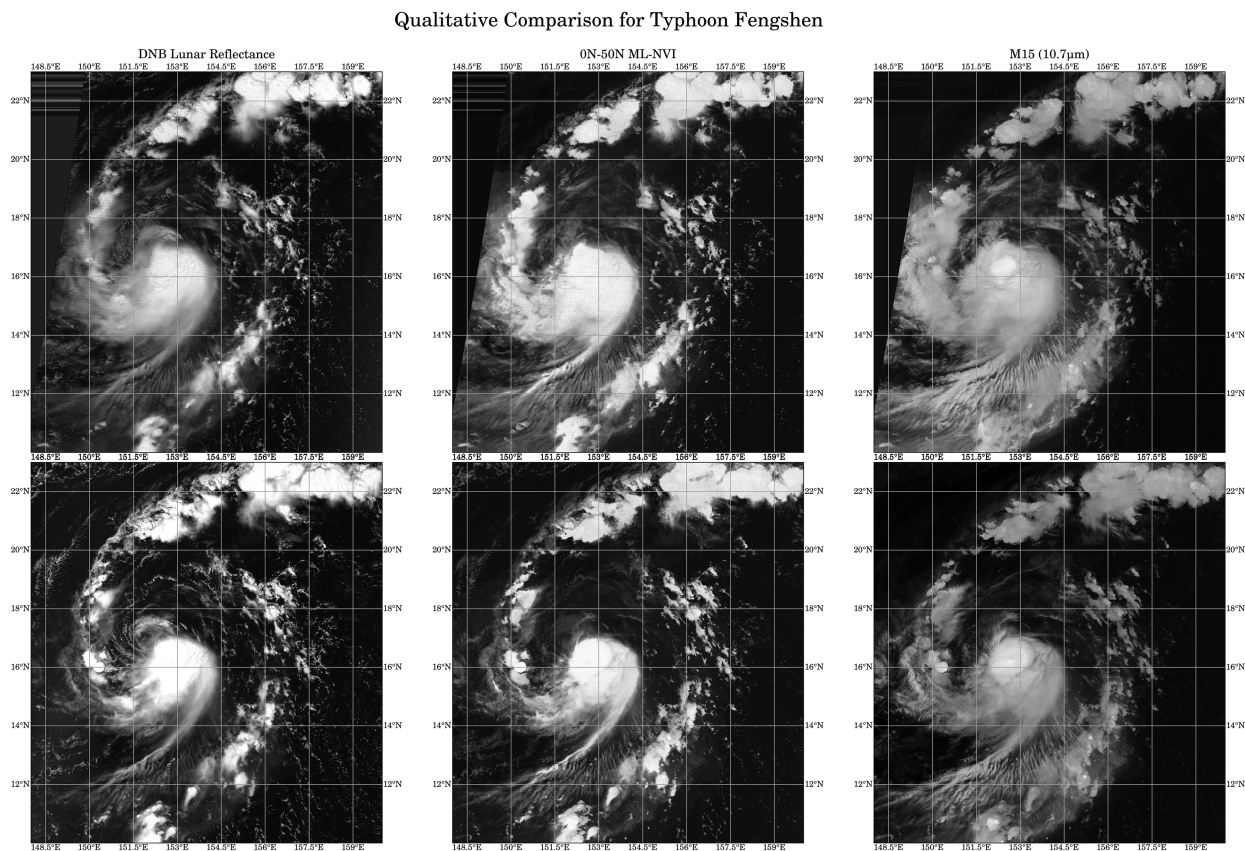


FIG. 11. Qualitative comparisons (left to right) of images from DNB radiance calculated lunar reflectance, predicted lunar reflectance for the full-latitude model, and VIIRS M15 ($10.76\ \mu\text{m}$). Images are from two consecutive passes over Typhoon Fengshen in the West Pacific Ocean on (top) 1438 UTC 13 Nov 2019 and (bottom) 1529 UTC.

techniques and may also aid in minimizing false alarms for cloud products. While geostationary satellites are often the preferred imagery to use for cyclone and fog forecasting, there are observing and forecasting benefits to using polar orbiter imagery for these events as well. The secondhand impacts to aviation safety are vast. These examples demonstrate the use of NVI and benefits it can bring on the JPSSs if made available in real time. Hillger et al. (2016) stated that the “operational applications of this nighttime imagery are the ultimate validation of its usefulness,” and we have demonstrated the usefulness of the ML-NVI for low cloud identification with a focus on tropical cyclones and fog. Once the ML-NVI algorithm can be repurposed to run in near-real time, imagery can be distributed for use to a wide range of forecasters giving greater accessibility to the product.

The ML-NVI was designed as a proof of concept to demonstrate that measurements derived from IR channels common to both VIIRS and geostationary sensors, such as the ABI and Advanced Himawari Imager (AHI), can be used to create pseudo-lunar reflectances like those from measured DNB radiances—in an environment where there is ample validation data to test the performance. We have demonstrated both qualitatively and quantitatively the ability to create visually

consistent nighttime visible imagery from LWIR across the full lunar cycle. Ongoing research shows that the methodology and models used for JPSS VIIRS ML-NVI do translate to ABI and AHI sensors (Pasillas 2024, Pasillas et al. 2023, Stanford et al. 2024). This will enable persistent nighttime visible imagery via geostationary satellites for enhanced TC monitoring and more precise visualization of fog coverage extent to aid in the timing of fog formation and dissipation over a region or site. Details on this transfer will be covered in a follow-on paper.

Acknowledgments. This work was supported in part by the U.S. Air Force and the Office of Naval Research Award N000142012069. We thank Steve Reising, Kristen Rasmussen, and our anonymous reviewers for their comments.

Data availability statement. The dataset for this study was downloaded from NOAA Class and is publicly available at (<https://www.avl.class.noaa.gov>). Code for data preparation and access to the machine learning models is available by request to the corresponding author via email or at (<https://github.com/c-pasillas>). The Miller–Turner lunar reflectance model is available by request from CIRA.

REFERENCES

- Ackerman, S. A., K. I. Strabala, W. P. Menzel, R. A. Frey, C. C. Moeller, and L. E. Gumley, 1998: Discriminating clear sky from clouds with MODIS. *J. Geophys. Res.*, **103**, 32 141–32 157, <https://doi.org/10.1029/1998JD200032>.
- Anthis, A. I., and A. P. Cracknell, 1999: Use of satellite images for fog detection (AVHRR) and forecast of fog dissipation (METEOSAT) over lowland Thessalia, Hellas. *Int. J. Remote Sens.*, **20**, 1107–1124, <https://doi.org/10.1080/014311699212876>.
- Bendix, J., 2002: A Satellite-based climatology of fog and low-level stratus in Germany and adjacent areas. *Atmos. Res.*, **64**, 3–18, [https://doi.org/10.1016/S0169-8095\(02\)00075-3](https://doi.org/10.1016/S0169-8095(02)00075-3).
- Calvert, C., and M. Pavolonis, 2010: GOES-R Advanced Baseline Imager (ABI) Algorithm Theoretical Basis Document ATBD for Low Cloud and Fog. NOAA-NESDIS Algorithm Theoretical Basis Doc., 63 pp., <https://www.star.nesdis.noaa.gov/goesr/docs/ATBD/Imagery.pdf>.
- Chapman, R., and R. Gasparovic, 2022: *Remote Sensing Physics: An Introduction to Observing Earth from Space*. John Wiley and Sons, 496 pp.
- Chirokova, G., J. A. Knaff, and J. L. Beven, 2018: Proxy visible satellite imagery. *Proc. 22nd Conf. on Satellite Meteorology and Oceanography*, Austin, TX, Amer. Meteor. Soc., 7.6, <https://ams.confex.com/ams/98Annual/webprogram/Paper334276.html>.
- , and Coauthors, 2023: ProxyVis—A proxy for nighttime visible imagery applicable to geostationary satellite observations. *Wea. Forecasting*, **38**, 2527–2550, <https://doi.org/10.1175/WAF-D-23-0038.1>.
- Ellrod, G. P., 1995: Advances in the detection and analysis of fog at night using GOES multispectral infrared imagery. *Wea. Forecasting*, **10**, 606–619, [https://doi.org/10.1175/1520-0434\(1995\)010<0606:AITDAA>2.0.CO;2](https://doi.org/10.1175/1520-0434(1995)010<0606:AITDAA>2.0.CO;2).
- , and I. Gultepe, 2007: Inferring low cloud base heights at night for aviation using satellite infrared and surface temperature data. *Fog and Boundary Layer Clouds: Fog Visibility and Forecasting*, I. Gultepe, Ed., Birkhäuser, 1193–1205, https://doi.org/10.1007/978-3-7643-8419-7_6.
- Gurka, J. J., 1978a: The role of inward mixing in the dissipation of fog and stratus. *Mon. Wea. Rev.*, **106**, 1633–1635, [https://doi.org/10.1175/1520-0493\(1978\)106<1633:TROIMI>2.0.CO;2](https://doi.org/10.1175/1520-0493(1978)106<1633:TROIMI>2.0.CO;2).
- , 1978b: The use of enhanced visible imagery for predicting the time of fog dissipation. Preprints, *Conf. on Weather Forecasting and Analysis and Aviation Meteorology*, Washington, DC, National Oceanic and Atmospheric Administration, 343–346.
- Harder, P., and Coauthors, 2020: NightVision: Generating nighttime satellite imagery from infra-red observations. arXiv, 2011.07017v2, <https://doi.org/10.48550/arXiv.2011.07017>.
- Hillger, D., and Coauthors, 2016: User validation of VIIRS satellite imagery. *Remote Sens.*, **8**, 11, <https://doi.org/10.3390/rs8010011>.
- Hillger, D. W., 2008: GOES-R advanced baseline imager color product development. *J. Atmos. Oceanic Technol.*, **25**, 853–872, <https://doi.org/10.1175/2007JTECHA911.1>.
- Hoese, D., W. Roberts, E. Schiffer, K. Strabala, J. Feltz, R. K. Garcia, and J. Zeng, 2023: ssec/polar2grid: Python package version 3.0.2. Zenodo, <https://doi.org/10.5281/zenodo.7662308>.
- Hogan, R. J., E. J. O'Connor, and A. J. Illingworth, 2009: Verification of cloud-fraction forecasts. *Quart. J. Roy. Meteor. Soc.*, **135**, 1494–1511, <https://doi.org/10.1002/qj.481>.
- Inoue, T., 1989: Features of clouds over the tropical Pacific during northern hemispheric winter derived from split window measurements. *J. Meteor. Soc. Japan*, **67**, 621–637, https://doi.org/10.2151/jmsj1965.67.4_621.
- Kidder, S. Q., and T. H. Vonder Haar, 1995: *Satellite Meteorology: An Introduction*. Gulf Professional Publishing, 466 pp.
- , D. W. Hillger, A. J. Mostek, and K. J. Schrab, 2000: Two simple GOES imager products for improved weather analysis and forecasting. *Natl. Wea. Dig.*, **24**, 25–30.
- Kieffer, H. H., and T. C. Stone, 2005: The spectral irradiance of the moon. *Astron. J.*, **129**, 2887–2901, <https://doi.org/10.1086/430185>.
- Kim, H.-W., J.-M. Yeom, D. Shin, S. Choi, K.-S. Han, and J.-L. Roujean, 2017: An assessment of thin cloud detection by applying bidirectional reflectance distribution function model-based background surface reflectance using Geostationary Ocean Color Imager (GOCI): A case study for South Korea. *J. Geophys. Res. Atmos.*, **122**, 8153–8172, <https://doi.org/10.1002/2017JD026707>.
- Kim, J.-H., S. Ryu, J. Jeong, D. So, H.-J. Ban, and S. Hong, 2020: Impact of satellite sounding data on virtual visible imagery generation using conditional generative adversarial network. *IEEE J. Sel. Top. Appl. Earth Obs. Remote Sens.*, **13**, 4532–4541, <https://doi.org/10.1109/JSTARS.2020.3013598>.
- Kim, K., J.-H. Kim, Y.-J. Moon, E. Park, G. Shin, T. Kim, Y. Kim, and S. Hong, 2019: Nighttime reflectance generation in the visible band of satellites. *Remote Sens.*, **11**, 2087, <https://doi.org/10.3390/rs11182087>.
- Kim, Y., and S. Hong, 2019: Deep learning-generated nighttime reflectance and daytime radiance of the midwave infrared band of a geostationary satellite. *Remote Sens.*, **11**, 2713, <https://doi.org/10.3390/rs11222713>.
- Liang, C. K., S. Mills, B. I. Hauss, and S. D. Miller, 2014: Improved VIIRS day/night band imagery with near-constant contrast. *IEEE Trans. Geosci. Remote Sens.*, **52**, 6964–6971, <https://doi.org/10.1109/TGRS.2014.2306132>.
- Lin, L., and C. Cao, 2019: The effects of VIIRS detector-level and band-averaged relative spectral response differences between S-NPP and NOAA-20 on the thermal emissive bands. *IEEE J. Sel. Top. Appl. Earth Obs. Remote Sens.*, **12**, 4123–4130, <https://doi.org/10.1109/JSTARS.2019.2938221>.
- Lindsey, D. T., L. Grasso, J. F. Dostalek, and J. Kerkmann, 2014: Use of the GOES-R split-window difference to diagnose deepening low-level water vapor. *J. Appl. Meteor. Climatol.*, **53**, 2005–2016, <https://doi.org/10.1175/JAMC-D-14-0010.1>.
- Line, B., D. Hillger, and T. Kopp, 2018: Joint Polar Satellite System (JPSS) VIIRS Imagery Products Algorithm Theoretical Basis Document (ATBD) Revision E. NOAA NESDIS Algorithm Theoretical Basis Doc., 55 pp.
- Liou, K. N., 2002: *An Introduction to Atmospheric Radiation*. Vol. 84, Elsevier, 608 pp.
- Loew, A., and Coauthors, 2017: Validation practices for satellite-based Earth observation data across communities. *Rev. Geophys.*, **55**, 779–817, <https://doi.org/10.1002/2017RG000562>.
- Miller, S. D., and R. E. Turner, 2009: A dynamic lunar spectral irradiance data set for NPOESS/VIIRS day/night band nighttime environmental applications. *IEEE Trans. Geosci. Remote Sens.*, **47**, 2316–2329, <https://doi.org/10.1109/TGRS.2009.2012696>.
- , J. D. Hawkins, K. Richardson, T. F. Lee, and F. J. Turk, 2006: Enhanced tropical cyclone monitoring with MODIS and OLS. *Proc. 27th Conf. Hurricanes and Tropical Meteorology*, Monterey, CA, Amer. Meteor. Soc., 15A.6,

- <https://ams.confex.com/ams/27Hurricanes/webprogram/Paper108619.html>.
- , and Coauthors, 2013: Illuminating the capabilities of the Suomi National Polar-orbiting Partnership (NPP) Visible Infrared Imaging Radiometer Suite (VIIRS) day/night band. *Remote Sens.*, **5**, 6717–6766, <https://doi.org/10.3390/rs5126717>.
- , and Coauthors, 2022: A physical basis for the overstatement of low clouds at night by conventional satellite infrared-based imaging radiometer bi-spectral techniques. *Earth Space Sci.*, **9**, e2021EA002137, <https://doi.org/10.1029/2021EA002137>.
- Min, M., and Coauthors, 2017: An investigation of the implications of lunar illumination spectral changes for day/night band-based cloud property retrieval due to lunar phase transition. *J. Geophys. Res. Atmos.*, **122**, 9233–9244, <https://doi.org/10.1002/2017JD027117>.
- Mohandooss, T., A. Kulkarni, D. Northrup, E. Mwebaze, and H. Alejomhammad, 2020: Generating synthetic multispectral satellite imagery from Sentinel-2. arXiv, 2012.03108v1, <https://doi.org/10.48550/arXiv.2012.03108>.
- Pasillas, C., 2024: Turning night into day: The creation, validation, and application of synthetic lunar reflectance values from the day-night band and infrared sensors for use with JPSS VIIRS and GOES ABI. Ph.D. thesis, Colorado State University, 84 pp., <https://mountainscholar.org/items/4f016373-f867-40e3-b58b-aad51b503cb9>.
- , M. M. Bell, and C. D. Kummerow, 2023: Enhancing low level closed circulation identification using night-time visible imagery. *23rd Symp. on Meteorological Observation and Instrumentation*, Denver, CO, Amer. Meteor. Soc., 15A.3, <https://ams.confex.com/ams/103ANNUAL/meetingapp.cgi/Paper/419325>.
- Pedregosa, F., and Coauthors, 2011: Scikit-learn: Machine learning in Python. *J. Mach. Learn. Res.*, **12**, 2825–2830.
- Pitts, K., and M. Seybold, 2010: ABI L2 cloud and moisture imagery beta, provisional and full validation Readiness, Implementation and Management Plan (RIMP) V2. NOAA-NESDIS410-R-RIMP-0323, 31 pp.
- Prabhakara, C., R. S. Fraser, G. Dalu, M.-L. C. Wu, R. J. Curran, and T. Styles, 1988: Thin cirrus clouds: Seasonal distribution over oceans deduced from Nimbus-4 IRIS. *J. Appl. Meteor.*, **27**, 379–399, [https://doi.org/10.1175/1520-0450\(1988\)027<0379:TCCSDO>2.0.CO;2](https://doi.org/10.1175/1520-0450(1988)027<0379:TCCSDO>2.0.CO;2).
- Raspaud, M., and Coauthors, 2019: pytroll/satpy: Version 0.16.0. Zenodo, <https://doi.org/10.5281/zenodo.3250583>.
- Seaman, C., D. W. Hillger, T. J. Kopp, R. Williams, S. Miller, and D. Lindsey, 2015: Visible Infrared Imaging Radiometer Suite (VIIRS) Imagery Environmental Data Record (EDR) User's Guide Version 1.3. NOAA Tech Rep. NESDIS 150, 36 pp., <https://doi.org/10.7289/V5/TR-NESDIS-150>.
- Seaman, C. J., and S. D. Miller, 2015: A dynamic scaling algorithm for the optimized digital display of VIIRS day/night band imagery. *Int. J. Remote Sens.*, **36**, 1839–1854, <https://doi.org/10.1080/01431161.2015.1029100>.
- Stanford, N. K., C. Pasillas, and A. J. Wimmers, 2024: Center fixing tropical depressions and tropical storms using machine learning - nighttime visible imagery. *36th Conf. on Hurricanes and Tropical Meteorology*, Long Beach, CA, Amer. Meteor. Soc., 16D.3, <https://ams.confex.com/ams/36Hurricanes/meetingapp.cgi/Paper/441438>.
- Strabala, K. I., S. A. Ackerman, and W. P. Menzel, 1994: Cloud properties inferred from 8–12- μ m data. *J. Appl. Meteor.*, **33**, 212–229, [https://doi.org/10.1175/1520-0450\(1994\)033<0212:CPIFD>2.0.CO;2](https://doi.org/10.1175/1520-0450(1994)033<0212:CPIFD>2.0.CO;2).
- Warren, S. G., C. J. Hahn, J. London, R. M. Chervin, and R. L. Jenne, 1988: Global distribution of total cloud cover and cloud type amounts over the ocean. NCAR Tech. Note NCAR/TN-317+STR, 305 pp., <https://doi.org/10.2172/5415329>.
- Weiss, M., 2001: AVN-based MOS ceiling height and total sky cover guidance for the contiguous United States, Alaska, Hawaii and Puerto Rico. NWS Tech. Procedure Bull. 483, 22 pp.
- Wimmers, A. J., and C. S. Velden, 2016: Advancements in objective multisatellite tropical cyclone center fixing. *J. Appl. Meteor. Climatol.*, **55**, 197–212, <https://doi.org/10.1175/JAMC-D-15-0098.1>.
- Zhongming, Z., and Coauthors, 2012: Recommended methods for evaluating cloud and related parameters. WMO Tech. Rep. WWRP-2012-1, 40 pp.
- Zinke, S., 2017: A simplified high and near-constant contrast approach for the display of VIIRS day/night band imagery. *Int. J. Remote Sens.*, **38**, 5374–5387, <https://doi.org/10.1080/01431161.2017.1338838>.